



# Shifting modes of iron sulfidization at the onset of OAE-2 drive regional shifts in pyrite $\delta^{34}\text{S}$ records



R.N. Bryant<sup>a,b,\*</sup>, C. Jones<sup>a</sup>, M.R. Raven<sup>a,c</sup>, J.D. Owens<sup>d</sup>, D.A. Fike<sup>a</sup>

<sup>a</sup> Department of Earth & Planetary Sciences, Washington University in Saint Louis, St. Louis, MO 63130, USA

<sup>b</sup> Department of the Geophysical Sciences, University of Chicago, Chicago, IL 60637, USA

<sup>c</sup> Department of Earth Science, University of California, Santa Barbara, Santa Barbara, CA 93106, USA

<sup>d</sup> Department of Earth, Ocean and Atmospheric Science|National High Magnetic Field Laboratory, Florida State University, Tallahassee, FL 32306, USA

## ARTICLE INFO

Editor: Michael E. Böttcher

Keywords:

OAE-2

S isotopes

Fe sulfides

SIMS

Raman

Pyrite

Marcasite

## ABSTRACT

Total reduced inorganic S isotope ratios ( $\delta^{34}\text{S}_{\text{CRS}}$ ) shift toward more negative values across much of the southern North Atlantic just before the onset of the Cenomanian-Turonian Ocean Anoxic Event (OAE-2). At the same time, there is no parallel isotopic change in the significantly larger pool of kerogen (organic) S, which indicates that the distribution and S-isotope composition of sulfide in the environment likely did not drive the change in  $\delta^{34}\text{S}_{\text{CRS}}$ . Here, we investigate possible explanations for the negative shift in  $\delta^{34}\text{S}_{\text{CRS}}$  values and their divergence from organic S by isolating iron sulfides for morphological identification and grain-specific isotopic analysis using secondary ion mass spectrometry (SIMS). In pre- and *syn*-OAE-2 sedimentary rocks from Demerara Rise, we find four distinct morphologies of iron sulfides: pyrite framboids (1–20  $\mu\text{m}$  diameter), irregular pyrite aggregates (1–38  $\mu\text{m}$  diameter), large cemented pyrite aggregates (~60  $\mu\text{m}$  diameter), and irregular and cemented aggregates of the pyrite polymorph marcasite (1–45  $\mu\text{m}$  diameter). These different textural groups have distinct S-isotopic compositions that are largely consistent through the onset of OAE-2. As such, the secular change in bulk  $\delta^{34}\text{S}_{\text{CRS}}$  values likely reflects the changing proportions of these phases stratigraphically across OAE-2. All textural groups feature resolvable intra-grain  $\delta^{34}\text{S}$  variability, suggesting that the environments in which they formed were characterized by dynamic sulfide  $\delta^{34}\text{S}$  values and/or by partial closed-system distillation. We use grain-specific  $\delta^{34}\text{S}$  distributions to rule out shoaling of the chemocline within the sediments as a mechanism for the observed decrease in  $\delta^{34}\text{S}_{\text{CRS}}$ . Instead, we propose that changes in the reactivity of the iron species delivered to Demerara Rise over the ~200 kyr leading up to the onset of OAE-2 impacted the relative contributions of pyrite with S-isotope signatures reflecting the water column, shallow sediments, and deeper sediments to the bulk sedimentary  $\delta^{34}\text{S}_{\text{CRS}}$  value. Specifically, the change in iron reactivity at the onset of OAE-2 favored the production of  $^{34}\text{S}$ -depleted large, cemented aggregates and framboids at the expense of more  $^{34}\text{S}$ -enriched irregular aggregates. Our results underscore that bulk  $\delta^{34}\text{S}_{\text{CRS}}$  measurements integrate multiple reduced phases that form via distinct reaction mechanisms and potentially in different parts of the depositional environment. Grain-specific SIMS analyses dramatically enrich our ability to interpret pyrite isotopic patterns in the geologic record.

## 1. Introduction

The Cenomanian-Turonian Boundary Ocean Anoxic Event (OAE-2) was an interval of geographically extensive enhanced organic matter (OM) burial and  $\text{CO}_2$  drawdown, marked by a transient positive C isotope excursion in the marine organic and inorganic carbon records (Jarvis et al., 2011; Jenkyns, 2010; Owens et al., 2018; Trabucho Alexandre et al., 2010). The respiration of enhanced primary productivity is thought to have depleted oceanic oxygen concentrations

(Dickson et al., 2016; Ostrander et al., 2017; Owens et al., 2016, 2013; Schlanger and Jenkyns, 1976), leading to enhanced preservation of OM (Barron, 1983) and the formation of remarkably OM-rich sediments. At Demerara Rise, a site in the southern proto-North Atlantic (ODP 1258; Erbacher et al., 2005; Böttcher et al., 2006; Fig. 1), average pre-OAE-2 sediments contain 8.8 wt% TOC, whereas *syn*-OAE-2 sediments average 19 wt% TOC (Raven et al., 2019), partially due to lesser dilution by carbonates within the OAE-2 interval (Owens et al., 2016). One of the more unusual aspects of Demerara Rise is that Fe speciation and trace

\* Corresponding author at: Department of Earth & Planetary Sciences, Washington University in Saint Louis, St. Louis, MO 63130, USA.

E-mail address: [rbryant@uchicago.edu](mailto:rbryant@uchicago.edu) (R.N. Bryant).

<https://doi.org/10.1016/j.chemgeo.2020.119808>

Received 2 April 2020; Received in revised form 30 July 2020; Accepted 1 August 2020

Available online 06 August 2020

0009-2541/ © 2020 Elsevier B.V. All rights reserved.

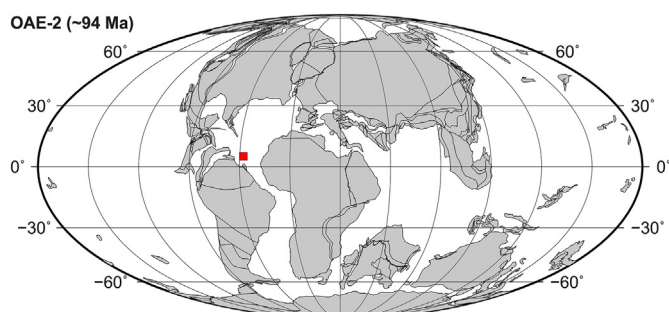


**Fig. 1.** Paleogeographic map during OAE-2 (~94 Ma) showing the location of the Demerara Rise (marked by the red square) in the proto-North Atlantic. Map generated using the ODSN Plate Tectonic Reconstruction Service (<http://www.odsn.de/odsn/services/paleomap/paleomap.html>). (For interpretation of the references to colour in this figure legend, the reader is referred to the web version of this article.)

metal geochemistry through OAE-2 indicate relatively stable, reducing local redox conditions (Böttcher et al., 2006; Hetzel et al., 2009; Owens et al., 2016). This is in sharp contrast to the interpreted global redox conditions, with oceanic deoxygenation during OAE-2, followed by minimal recovery in the wake of the event (Jenkyns, 2010; Ostrander et al., 2017; Owens et al., 2013).

Due to the intimate connection between the global C and S cycles (Bernier, 2001, 1989; Canfield, 2004; Fike et al., 2015; Garrels and Lerman, 1981), many have used the S-isotopic composition of different operationally defined S-bearing phases to probe the response of the global S cycle to OAE-2. S-isotopic compositions are expressed here in the standard delta notation (in units of permil, ‰) relative to the Vienna Canyon Diablo Troilite (VCDT) reference standard for S (Ding et al., 1999),

$$\delta^{34}\text{S}_{\text{sample}} = \left[ \frac{(^{34}\text{S}/^{32}\text{S})_{\text{sample}}}{(^{34}\text{S}/^{32}\text{S})_{\text{VCDT}}} - 1 \right] \times 1000 \quad (1)$$

The operationally defined pool of chromium-reducible S (CRS; Canfield et al., 1986) includes pyrite ( $\text{FeS}_2$ ), the pyrite polymorph marcasite ( $\text{FeS}_2$ ), and potentially elemental S ( $\text{S}^0$ ). The S-isotope composition of this pool ( $\delta^{34}\text{S}_{\text{CRS}}$ ) can provide insights into S cycling. The  $\delta^{34}\text{S}_{\text{CRS}}$  values at several sites in the southern proto-North Atlantic record a consistent  $\delta^{34}\text{S}$  pattern, in which they become more  $^{34}\text{S}$ -depleted over the ~200,000 years leading up to OAE-2 (Raven et al., 2019). Various factors have been suggested to have caused the decreasing  $\delta^{34}\text{S}_{\text{CRS}}$  before OAE-2, including chemocline migration (Gomes et al., 2016), increasing sulfur disproportionation (Hetzel et al., 2009; Kolonic et al., 2002), changes in the location of Fe sulfide formation in the environment (Raven et al., 2019), and declining oceanic sulfate concentration (Adams et al., 2010; Owens et al., 2013).

Recently, Raven et al. (2019) found that the S-isotopic composition of organic S ( $\delta^{34}\text{S}_{\text{OS}}$ ) at Demerara Rise was largely invariant before, during, and after OAE-2 with values ~0‰. As a result, the S-isotopic offset between CRS and organic S steadily increased leading up to OAE-2 (Fig. 2). The divergence of these two S isotope records provides clear constraints on the environmental changes impacting them. Interpreting the organic S pool as largely having formed through sulfurization of OM in the water column, Raven et al. (2019) suggested that the increasing offset between  $\delta^{34}\text{S}_{\text{CRS}}$  and  $\delta^{34}\text{S}_{\text{OS}}$  at Demerara Rise reflected an increase in the range of depths Fe sulfides formed, from primarily in the water column before OAE-2 to forming in both the water column and sediment pore waters during OAE-2. Such a scenario would require a change in the mineralogy of the Fe reaching the site, such that the relative importance of different pyrite formation mechanisms changed. Other observations further indicate that metal cycling at Demerara Rise was perturbed during OAE-2. Most notable is the shift in trace metals over the same time interval as the  $\delta^{34}\text{S}_{\text{CRS}}$  shift; Zn and V

concentrations drop, interpreted to reflect regional drawdown (Owens et al., 2016). Mo decreases in abundance shortly thereafter, demonstrating the sensitivity of oceanic metals cycling to a global and stepwise expansion of reducing environments. Additionally, total iron abundance is roughly two times higher during OAE-2 than before OAE-2 (Owens et al., 2012), and the median abundance of Fe sulfides in the carbonate-free fraction of Demerara Rise sediments is slightly higher during OAE-2 than before OAE-2 (Raven et al., 2019; Fig. A1, Appendix A). The proportion of Fe classed as highly reactive (including pyrite) is slightly lower during OAE-2 than before OAE-2 (Böttcher et al., 2006; Owens et al., 2016; Fig. 2), although it remains high throughout, indicating dominantly euxinic bottom waters.

$\delta^{34}\text{S}_{\text{CRS}}$  values can reflect variable contributions by multiple generations of mineral growth (Cui et al., 2018) and can be further complicated by the presence of multiple mineralogies (e.g., pyrite and marcasite; Bryant et al., 2019). Sulfide minerals record an integrated value representing the  $\delta^{34}\text{S}$  of aqueous sulfide during their formation. Recorded  $\delta^{34}\text{S}_{\text{CRS}}$  values can thus reflect local environmental factors (e.g., the ‘openness’ of the environment of mineral formation with respect to sulfate, or the abundance and reactivity of iron minerals; Bryant et al., 2019; Fike et al., 2015) and ecological factors [e.g., the magnitude of the biological fractionation associated with microbial sulfate reduction,  $\epsilon_{\text{mic}}$  (Leavitt et al., 2013; Sim et al., 2011b, 2011a; Wing and Halevy, 2014)]. Additionally, late-stage fluids can produce highly  $^{34}\text{S}$ -enriched pyrites, often with irregular textures such as overgrowths and cements (Berelson et al., 2018; Bryant et al., 2019; Cui et al., 2018; Raiswell, 1982). Any single or a combination of these factors could have contributed to the observed  $\delta^{34}\text{S}_{\text{CRS}}$  decrease toward the onset of OAE-2 at Demerara Rise and cannot be ruled out based on bulk  $\delta^{34}\text{S}_{\text{CRS}}$  data alone. However, the lack of substantive change within the organic S signal suggests that any perturbation likely impacted the timing or locus of Fe sulfide formation rather than inherent changes to S cycling.

Pinpointing the driver(s) of the decrease in  $\delta^{34}\text{S}_{\text{CRS}}$  values toward the onset of OAE-2 at Demerara Rise will provide important information about changes to the regional biogeochemical cycles of C, S, and Fe leading up to and during OAE-2. Here, we use spatially resolved S isotope analyses to assess regional C, S, and Fe cycling. A scanning ion imaging method of secondary ion mass spectrometry (SIMS) was recently developed for microcrystalline Fe sulfides, making it possible to investigate both inter- and intra-grain variability within the CRS pool (Bryant et al., 2019). By applying this method in a comparative study of Fe sulfides from pre- and *syn*-OAE-2 sediments at Demerara Rise, we can establish the various contributions to and mechanisms responsible for the observed secular decrease in  $\delta^{34}\text{S}_{\text{CRS}}$  values.

## 2. Methods & materials

### 2.1. Samples

We obtained three shale (squeeze cake) samples from ODP Site 1258 (drilled at a modern water depth of 3192.2 m, near the base of the western slope of Demerara Rise). The samples are highly OM-rich laminated mudstones from 402.32, 399.545, and 397.82 m below the sea floor (mbsf) which equates to 429.39, 426.62 and 422.78 m composite depth (mcd) [after Erbacher et al., 2005 and MacLeod et al., 2008]. Sample I.D. information is provided in Appendix A (Table A1). For reference, the OAE-2 interval occurs between ~426 and ~422 mcd (Erbacher et al., 2005; MacLeod et al., 2008; Owens et al., 2016). The mudstones were previously interpreted to have been deposited at a rate of ~1 cm/kyr beneath a water column with oxygen minimum zone (OMZ)-like upwelling and dominantly euxinic (anoxic, sulfide rich) bottom waters throughout OAE-2 (Böttcher et al., 2006; Hetzel et al., 2009; Owens et al., 2016). It should be noted that the stratigraphic resolution of this sampling is low and the sample within the OAE is from the returning limb of the C isotope excursion.

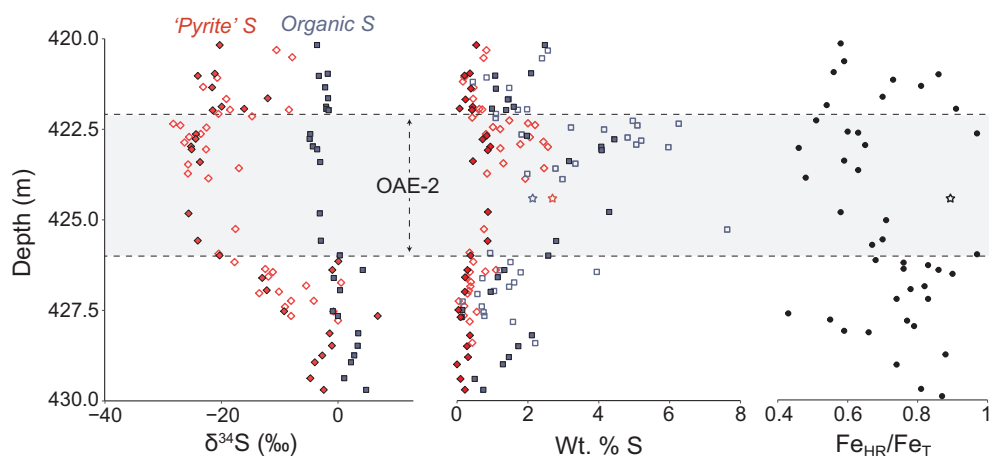


**Fig. 2.** Bulk S-isotopic compositions and abundances of 'pyrite' S (CRS) and organic S enveloping OAE-2 at Demerara Rise, after Böttcher et al. (2006) (open stars), Hetszel et al. (2009) (open diamonds and squares), and Raven et al. (2019) (filled diamonds and squares), and highly reactive iron to total iron ratios, after Böttcher et al. (2006) (open stars) and Owens et al. (2016) (filled circles). Note the presence of several 'outlying' more positive  $\delta^{34}\text{S}_{\text{CRS}}$  values that are not expressed in the organic S record, perhaps suggesting that the inorganic sulfur pool has a more complicated formation history than the organic S.

## 2.2. Extraction of Fe sulfides

A ShatterBox (SPEX, Metuchen, NJ) was utilized to powder 1 g of each sample for no longer than 1 min. Carbonate minerals were removed by three sequential 10-min treatments with 6 M hydrochloric acid, before the insoluble residue was rinsed five times with deionized water and dried in an oven at 60 °C for 24 h. The insoluble residues were then powdered by mortar and pestle. For each sample, a 0.25 g aliquot of insoluble residue powder was added to 45 mL of Lithium Polytungstate Heavy Liquid (LST) in a 50-mL centrifuge tube. The contents of these tubes were mixed for 1 min using a vortex mixer, then placed in an ultrasonic bath (35 kHz) for 15 min to de-flocculate the powders. Following Bryant et al. (2019), the tubes were spun in a centrifuge for 38 min at 3000 rpm to allow Fe sulfide grains of diameters  $\geq 0.5 \mu\text{m}$  to settle out, thus maintaining the original size distribution of iron sulfide grains. After centrifugation, heavy fractions were removed from the tubes using a plastic micropipette, placed in new 50-mL centrifuge tubes, rinsed, and centrifuged (5 min at 2000 rpm) five times in deionized water, and dried overnight at 60 °C in a vacuum oven.

## 2.3. Imaging

For each sample, Fe sulfide grains were mounted in 1-inch rounds of epoxy, along with fragments of the in-house marcasite and pyrite S-isotopic standards, and polished to 1  $\mu\text{m}$ , as in Bryant et al. (2019). Epoxy mounts were imaged using reflected light optical microscopy (2.5 $\times$  objective for stitched image used for SIMS stage calibration, 50–80 $\times$  for regions of interest). For the *syn*-OAE-2 sample (422.78 m), representative Fe sulfide aggregates were previously imaged by Scanning Electron Microscopy (SEM) in Bryant et al. (2019).

## 2.4. Laser Raman microprobe analysis

The mineralogy of all Fe sulfide grains in regions of interest of the epoxy puck were confirmed using laser Raman microprobe analysis (1 mW laser power, 80 $\times$  objective, 20 analyses of 1 s duration, as in Bryant et al. (2018)). All Fe sulfide grains present were either pyrite or marcasite, and thus were easily distinguishable based on the positions of the two dominant bands in Raman spectra obtained: marcasite has prominent bands at  $\sim 324$  and  $\sim 387 \Delta\text{cm}^{-1}$ , whereas pyrite has prominent bands at  $\sim 343$  and  $\sim 379 \Delta\text{cm}^{-1}$  (Bryant et al., 2018).

## 2.5. SIMS S isotope analyses

We used fragments of hydrothermal pyrite and marcasite crystals, both previously demonstrated to be isotopically homogeneous and

calibrated against Balmat pyrite (Bryant et al., 2019), as S-isotopic standards in SIMS experiments. Following Bryant et al. (2019), environmental Fe sulfide grains were pre-sputtered by  $\text{Cs}^+$  bombardment for 300 s with a 1 nA beam current at raster sizes at least several microns larger than the exposed grains (20–80  $\mu\text{m}$ ). S-isotopic ratio analyses were then performed in scanning ion imaging mode by  $\text{Cs}^+$  bombardment (beam diameter of  $< 1 \mu\text{m}$ , current of  $\sim 10 \text{ pA}$ ) of the same raster squares using an electron multiplier (EM) detector on a IMS 7f-GEO SIMS instrument (CAMECA, Fitchburg, WI, USA) at Washington University in Saint Louis (St Louis, MO, USA) to collect counts of  $^{32}\text{S}^-$  and  $^{34}\text{S}^-$  for each pixel (grids of 128  $\times$  128 pixels) between 20 and 480 planes (1 min per plane). In post-processing, raw isotope ratios were calculated by taking the mean  $^{34}\text{S}^-/^{32}\text{S}^-$  ion count ratio of a central area of each grain integrated over all analysis planes. Various corrections were applied to the data, including a dead-time correction, an interpolation of  $^{34}\text{S}^-$  counts to align in time with those on  $^{32}\text{S}^-$ , and a quasi-simultaneous arrival (QSA) effect correction (Bryant et al., 2019; Jones et al., 2017). Finally, instrumental mass fractionation was then corrected for by calculating the mineral-specific fractionation factor ( $^{34}\alpha$ ) based on the mean raw (from SIMS) and known  $\delta^{34}\text{S}$  value of the population of internal hydrothermal pyrite or marcasite standards and dividing the average  $^{34}\text{S}^-/^{32}\text{S}^-$  ratio of each environmental Fe sulfide grain by the appropriate value of  $^{34}\alpha$ . The grain-to-grain reproducibility for this method ( $n = 14$ ,  $1\sigma$ ) was previously reported to be  $\pm 1.9\text{‰}$  for 1–3- $\mu\text{m}$ -diameter fragments of hydrothermal pyrite (Bryant et al., 2019).

## 3. Results

### 3.1. Fe sulfide minerals and textures

Optical microscopy and laser Raman microprobe analyses suggested that all density-separated samples contained exclusively Fe sulfide minerals, which can be grouped as follows: (i) pyrite framboids ( $\sim 1$ – $20 \mu\text{m}$  spheroidal to sub-spheroidal clusters of equidimensional and equimorphic pyrite microcrystals; Ohfuji and Rickard, 2005; Fig. 3A–C), (ii) irregular pyrite aggregates (microscopic non-spheroidal clusters of pyrite microcrystals,  $\sim 1$ – $38 \mu\text{m}$ ; Fig. 3D–H), (iii) cemented pyrite aggregates (angular pyrite aggregates in which microcrystals are challenging to discern due to pyritic cementation; Fig. 3I), and (iv) marcasite (as aggregates of intergrown euhedral microcrystals, or as fully cemented aggregates,  $\sim 1$ – $45 \mu\text{m}$ ; Fig. 3J, K).

By assuming that every Fe sulfide grain imaged is roughly spherical and non-porous, and cut directly through its equator (Jones et al., 2019), we can approximate the relative proportions of the different Fe sulfide groups in each sample – these are summarized in Table 1, and in Fig. 4A. Average pyrite framboid sizes are  $\sim 10 \mu\text{m}$  prior to OAE-2 and

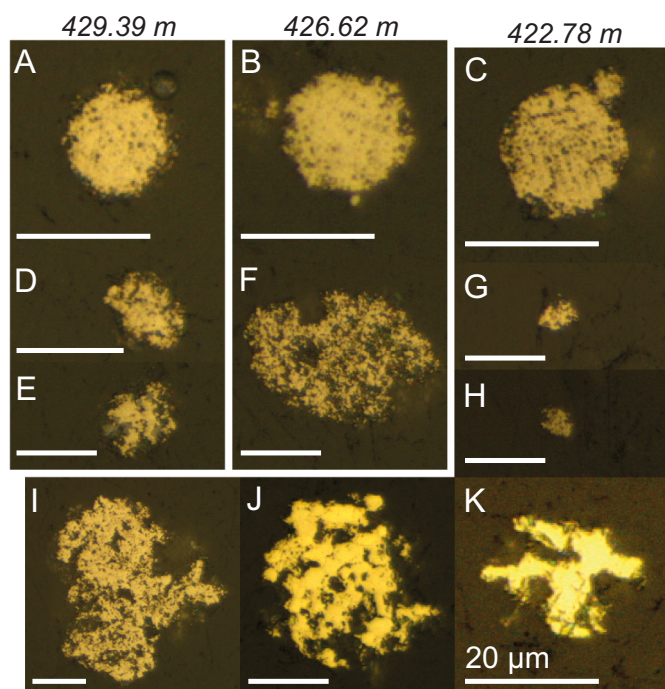


**Fig. 3.** Reflected light optical microscope images (all scale bars are 20  $\mu\text{m}$ ) of different Fe sulfide minerals and textures from Demerara Rise samples. (A–C) in-filled pyrite framboids from depths of 429.39 (pre-OAE-2), 426.62 (pre-OAE-2) and 422.78 m (syn-OAE-2); (D–H) irregular pyrite aggregates from depths of 429.39 (D–E), 426.62 (F) and 422.78 m (G–H); (I) cemented pyrite aggregate from a depth of 422.78 m, and (J–K) marcasite from a depth of 422.78 m.

smaller ( $\sim 4 \mu\text{m}$ ) during OAE-2 (Table 1).

In our samples, the proportion of  $\text{FeS}_2$  present as pyrite framboids appears to decline leading into OAE-2, while the proportion as irregular pyrite aggregates also decreases. Marcasite and large cemented pyrite aggregates are volumetrically dominant in the syn-OAE-2 sample.

### 3.2. SIMS S isotope analyses

#### 3.2.1. Inter-grain $\delta^{34}\text{S}$ variability

Grain-specific  $\delta^{34}\text{S}$  values obtained using SIMS scanning ion imaging (Table A2, Appendix A) reflect the integrated value for the exposed cross-sectional areas of polished grains (Bryant et al., 2019; Jones et al., 2019); although these multiple-image-plane analyses integrate depth somewhat, the  $\delta^{34}\text{S}$  values reported in this section may not always be representative of the integrated value of the entire grain. Regardless, in all samples, pyrite framboids and irregular pyrite aggregates appear to be the most  $^{34}\text{S}$ -depleted and  $^{34}\text{S}$ -enriched textural groups, respectively (Fig. 4A). Neither group's isotopic composition shows strong stratigraphic variability, each differing by less than 8‰ between the three samples.

In the deepest sample (429.39 m; pre-OAE-2), pyrite framboids have a minimum  $\delta^{34}\text{S}$  value of  $-36.1 \pm 0.8\text{‰}$  (1 standard error, s.e.; Fig. 4A, B), an average  $\delta^{34}\text{S}$  value of  $-21.5 \pm 8.9\text{‰}$  (1 standard deviation,  $\sigma$ ;  $n = 18$ ; Fig. 4A, B), and a maximum  $\delta^{34}\text{S}$  value of

$+0.4 \pm 0.8\text{‰}$  (1 s.e.; Fig. 4A, B). Irregular pyrite aggregates have a minimum  $\delta^{34}\text{S}$  value of  $-18.3 \pm 0.8\text{‰}$  (1 s.e.; Fig. 4A), an average  $\delta^{34}\text{S}$  value of  $-4.9 \pm 10.5\text{‰}$  ( $1\sigma$ ;  $n = 6$ ; Fig. 4A), and a maximum  $\delta^{34}\text{S}$  value of  $+11.3 \pm 0.9\text{‰}$  (1 s.e.; Fig. 4A).

In the sample deposited slightly before OAE-2 (426.62 m), pyrite framboids have a minimum  $\delta^{34}\text{S}$  value of  $-36.2 \pm 1.1\text{‰}$  (1 s.e.; Fig. 4A, B), an average  $\delta^{34}\text{S}$  value of  $-26.0 \pm 5.6\text{‰}$  ( $1\sigma$ ;  $n = 8$ ; Fig. 4A, B), and a maximum  $\delta^{34}\text{S}$  value of  $-18.9 \pm 0.6\text{‰}$  (1 s.e.; Fig. 4A, B). Irregular pyrite aggregates have a minimum  $\delta^{34}\text{S}$  value of  $-16.0 \pm 1.7\text{‰}$  (1 s.e.; Fig. 4A), an average  $\delta^{34}\text{S}$  value of  $-12.8 \pm 2.6\text{‰}$  ( $1\sigma$ ;  $n = 4$ ; Fig. 4A), and a maximum  $\delta^{34}\text{S}$  value of  $-9.8 \pm 0.4\text{‰}$  (1 s.e.; Fig. 4A).

The sample deposited during OAE-2 (422.78 m) contains abundant cemented aggregates and marcasite in addition to the framboids and irregular aggregates observed throughout. Pyrite framboids at 422.78 m have a minimum  $\delta^{34}\text{S}$  value of  $-37.4 \pm 3.7\text{‰}$  (1 s.e.; Fig. 4A, B), an average  $\delta^{34}\text{S}$  value of  $-28.3 \pm 6.0\text{‰}$  ( $1\sigma$ ;  $n = 35$ ; Fig. 4A, B) and a maximum  $\delta^{34}\text{S}$  value of  $-13.2 \pm 1.0\text{‰}$  (1 s.e.; Fig. 4A, B). Irregular pyrite aggregates have a minimum  $\delta^{34}\text{S}$  value of  $-18.4 \pm 0.5\text{‰}$  (1 s.e.; Fig. 4A), an average  $\delta^{34}\text{S}$  value of  $-11.8 \pm 6.0\text{‰}$  ( $1\sigma$ ;  $n = 3$ ; Fig. 4A), and a maximum  $\delta^{34}\text{S}$  value of  $-6.8 \pm 2.1\text{‰}$  (1 s.e.; Fig. 4A). In the same sample, most marcasites have  $\delta^{34}\text{S}$  values closer to those of the framboids, with a minimum  $\delta^{34}\text{S}$  value of  $-33.9 \pm 6.6\text{‰}$  (1 s.e.; Fig. 4A) and an average  $\delta^{34}\text{S}$  value of  $-23.9 \pm 11.8\text{‰}$  ( $1\sigma$ ;  $n = 20$ ; Fig. 4A). The most  $^{34}\text{S}$ -enriched marcasite, however, has a  $\delta^{34}\text{S}$  value of  $+18.9 \pm 2.0\text{‰}$  (1 s.e.; Fig. 4A). Finally, a single large ( $\sim 60 \mu\text{m}$ ) cemented pyrite aggregate has a  $\delta^{34}\text{S}$  value of  $-19.0 \pm 0.1\text{‰}$  (1 s.e.; Fig. 4A).

Assuming an averaged SIMS  $\delta^{34}\text{S}$  value is representative of each mineral fabric (not every specific grain was analyzed via SIMS), a volume-adjusted SIMS  $\delta^{34}\text{S}$  value can be estimated for the Fe sulfides imaged from each sample. Volume-adjusted  $\delta^{34}\text{S}$  values are  $-10.5$ ,  $-14.7$ , and  $-21.8\text{‰}$  for the samples from depths of 429.39, 426.62, and 422.78 m, respectively (Table 2). These values are comparable to the previously reported bulk  $\delta^{34}\text{S}_{\text{CRS}}$  values ( $-4.7$ ,  $-13.0$ , and  $-24.4\text{‰}$ ; Table 2; Raven et al., 2019), suggesting that our subset of physically extracted Fe sulfides analyzed by SIMS are broadly representative of bulk Fe sulfides in the samples.

#### 3.2.2. Intra-grain $\delta^{34}\text{S}$ variability

To understand the system(s) in which the different Fe sulfide textures formed, it can be useful to probe intra-grain  $\delta^{34}\text{S}$  variability (Bryant et al., 2019; Cui et al., 2018). Using our  $^{32}\text{S}^-$  and  $^{34}\text{S}^-$  ion images of Fe sulfides from Demerara Rise, we now investigate intra-grain isotopic variability across multiple  $\sim 1$ – $5 \mu\text{m}$  diameter regions within individual Fe sulfides representing all Fe sulfide textures identified in these samples. In some cases, there may be indiscernible variability that occurs on scales smaller than the size of the primary beam ( $\sim 0.5 \mu\text{m}$ ) or with a magnitude smaller than the precision of individual measurements. To ensure that the apparent intra-grain variability is larger than that which would be expected based on the precision of the method, we always compare the standard deviation of intra-grain measurements to the average standard error over cycles associated with individual intra-grain measurements (Bryant et al., 2019). Where variations in  $\delta^{34}\text{S}$  can be discerned within individual grains, we test for spatial autocorrelation using global Moran's I. We

**Table 1**

Framboid sizes, and relative abundances of different Fe sulfide minerals and textures in the three samples from Demerara Rise, as inferred from optical microscopy and laser Raman microprobe analysis. The samples from depths of 429.39 and 426.62 m are pre-OAE-2 and the sample from a depth of 422.78 m is syn-OAE-2.

Sample depth (m)	Mean framboid size ( $\mu\text{m}$ )	Vol% pyrite framboids	Vol% irregular pyrite	Vol% cemented pyrite aggregates	Vol% marcasite
422.78	$4.2 \pm 3.4$ ( $1\sigma$ )	3.5	0.1	63.0	33.3
426.62	$10.3 \pm 4.2$ ( $1\sigma$ )	16.5	83.5	0	0
429.39	$9.6 \pm 3.3$ ( $1\sigma$ )	32.5	67.5	0	0

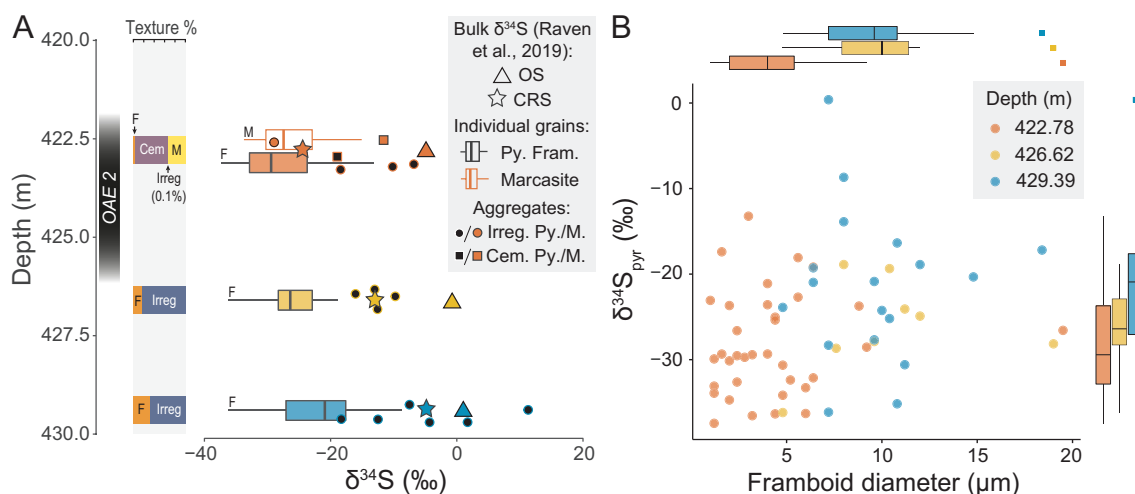


**Fig. 4.** Records of Fe sulfide texture/mineralogy and S-isotope change through OAE-2 at Demerara Rise. (A) Proportions of different Fe sulfide minerals/textures (F = pyrite framboid, Irreg = irregular pyrite aggregate, Cem = cemented pyrite aggregate, M = marcasite); black outline box and whisker plots (F) are for pyrite framboid SIMS  $\delta^{34}\text{S}$ , orange outline box and whisker plot (M) is for individual marcasite grain SIMS  $\delta^{34}\text{S}$ ; jittered black circles are irregular pyrite aggregate SIMS  $\delta^{34}\text{S}$  values, the black square is the SIMS  $\delta^{34}\text{S}$  value of a cemented pyrite aggregate, the orange circle is the SIMS  $\delta^{34}\text{S}$  value of an irregular marcasite aggregate, and the orange square is the SIMS  $\delta^{34}\text{S}$  value of a cemented marcasite aggregate; black-outlined stars and triangles are the  $\delta^{34}\text{S}_{\text{CRS}}$  and  $\delta^{34}\text{S}_{\text{OS}}$  values, respectively, for the samples used in this study, from Raven et al. (2019). (B) Cross plot of pyrite framboid SIMS  $\delta^{34}\text{S}$  values vs. their diameters, with marginal box and whisker plots, where squares are outliers; there is no consistent relationship between framboid size and  $\delta^{34}\text{S}$  value.

**Table 2**

Volume-adjusted Fe sulfide- $\delta^{34}\text{S}$  values (this study) compared with bulk CRS- and OS- $\delta^{34}\text{S}$  values from Raven et al. (2019). The samples from depths of 429.39 and 426.62 m are pre-OAE-2 and the sample from a depth of 422.78 m is syn-OAE-2.

Sample depth (mcd)	Volume-adjusted Fe sulfide $\delta^{34}\text{S}$ (‰)	$\delta^{34}\text{S}_{\text{CRS}}$ (‰)	$\delta^{34}\text{S}_{\text{OS}}$ (‰)
422.78	-21.8	-24.4	-4.9
426.62	-14.7	-13.0	-0.7
429.39	-10.5	-4.7	1.1

also test for linear correlation between the distance of the center of regions of interest from the nearest grain edge and their  $\delta^{34}\text{S}$  values (see an explanation of both tests in Appendix A, page 9).

**3.2.2.1. Pyrite framboids.** For all three samples, pyrite framboids > 4  $\mu\text{m}$  in diameter feature discernible intra-grain  $\delta^{34}\text{S}$  variability (Fig. 5), the clearest cases of which form spatial trends similar to those seen in cm-scale pyrite structures, for example, core-rim  $^{34}\text{S}$ -enrichments in Archean-age pyrite nodules (Fischer et al., 2014), exoskeleton-appendage  $^{34}\text{S}$ -enrichments in Ordovician-age pyritized trilobites (Briggs et al., 1991), and centripetal  $^{34}\text{S}$ -enrichments in Ediacaran pyritized *Conotubus* fossils (Schiffbauer et al., 2014), but never previously observed in framboids. Although some grains show intra-grain variation in  $^{32}\text{S}^-$  ion counts, there are no strong trends between counts and  $\delta^{34}\text{S}$  (Fig. A2, Appendix A). There is a positive correlation between the mean  $\delta^{34}\text{S}$  value of a framboid and the standard deviation of intra-grain  $\delta^{34}\text{S}$  measurements in the horizontal (x-y) plane (Fig. A3, Appendix A). In the deepest sample (429.39 m), pyrite framboids are mostly infilled (i.e., individual microcrystals are only clearly visible toward the edges of framboids; Fig. 5A, B) and feature moderate intra-grain variation in  $\delta^{34}\text{S}$  (average  $1\sigma = \pm 4.5\%$ , compared to an average intra-grain standard error of  $\pm 2.1\%$ ,  $1\sigma$ ,  $n = 43$ ). A large framboid (Fig. 5A) features clear core-rim radial enrichments in  $^{34}\text{S}$  (Table A3, Appendix A). A smaller framboid (Fig. 5B) has a relatively  $^{34}\text{S}$ -enriched infilled central region and a relatively  $^{34}\text{S}$ -depleted, non-infilled outer region (Table A3, Appendix A). In the sample deposited slightly before OAE-2 (426.62 m), framboids are again mostly infilled (Fig. 5C, D) and feature moderate

intra-grain variation in  $\delta^{34}\text{S}$  (average  $1\sigma = \pm 5.6\%$ , compared to an average intra-grain standard error of  $\pm 2.5\%$ ,  $1\sigma$ ,  $n = 34$ ). A smaller framboid (Fig. 5C) displays no clear spatial trend in intra-grain  $\delta^{34}\text{S}$  values (Table A3, Appendix A), whereas a larger framboid (Fig. 5D) features clear core-rim radial enrichments in  $^{34}\text{S}$  (Table A3, Appendix A). In the sample deposited during OAE-2 (422.78 m), a small, partially infilled framboid (Fig. 5E) has negligible intra-grain variation in  $\delta^{34}\text{S}$  in the x-y plane ( $1\sigma = \pm 3.0\%$ , compared to an average intra-grain standard error of  $\pm 3.4\%$ ,  $1\sigma$ ,  $n = 10$ ; Table A3, Appendix A). In contrast, a larger infilled framboid (Fig. 5F) has clear core-rim radial enrichments in  $^{34}\text{S}$  ( $1\sigma = \pm 4.4\%$ , compared to an average intra-grain standard error of  $\pm 1.5\%$ ,  $1\sigma$ ,  $n = 30$ ; Table A3, Appendix A). Generally, where substantial isotopic variability can be discerned, it takes the form of radial enrichments in  $^{34}\text{S}$  that are visible in cross sections (e.g., Fig. 5A, D, and F). These patterns are representative for the populations of framboids in all the samples studied.

**3.2.2.2. Irregular pyrite aggregates.** As with the pyrite framboids, irregular pyrite aggregates from all three samples feature discernible intra-grain  $\delta^{34}\text{S}$  variability. In some cases, this variability again takes the form of core-rim  $^{34}\text{S}$  enrichments, but other patterns include positive spatial autocorrelation without radial trends. Although some grains show intra-grain variation in  $^{32}\text{S}^-$  ion counts, there is only a trend between counts and  $\delta^{34}\text{S}$  for one case (Figs. 6F; A4F, Appendix A) – this trend appears to be largely driven by two anomalously high-count regions sampled close to a rough grain edge. There is no correlation between the mean  $\delta^{34}\text{S}$  value of an irregular aggregate and the standard deviation of intra-grain  $\delta^{34}\text{S}$  measurements in the x-y plane (Fig. A3, Appendix A). In the deepest pre-OAE-2 sample (429.39 m), irregular pyrite aggregates (Fig. 6A–C) again feature substantial intra-grain variation in  $\delta^{34}\text{S}$  (average  $1\sigma = \pm 6.8\%$ , compared to an average intra-grain standard error of  $\pm 2.4\%$ ,  $1\sigma$ ,  $n = 47$ ). One of these aggregates (Fig. 6A) displays positive spatial autocorrelation (Table A3, Appendix A), two of these aggregates (Fig. 6A, C) feature relatively  $^{34}\text{S}$ -depleted cores and relatively  $^{34}\text{S}$ -enriched edges, (Table A3, Appendix A), whereas one (Fig. 6B) displays no clear spatial isotopic trend (Table A3, Appendix A). In the sample deposited slightly before OAE-2 (426.62 m), irregular pyrite aggregates (Fig. 6D–F) feature substantial intra-grain variation in  $\delta^{34}\text{S}$  (average  $1\sigma = \pm 5.5\%$ , compared to an average intra-grain standard error of  $\pm 2.1\%$ ,  $1\sigma$ ,

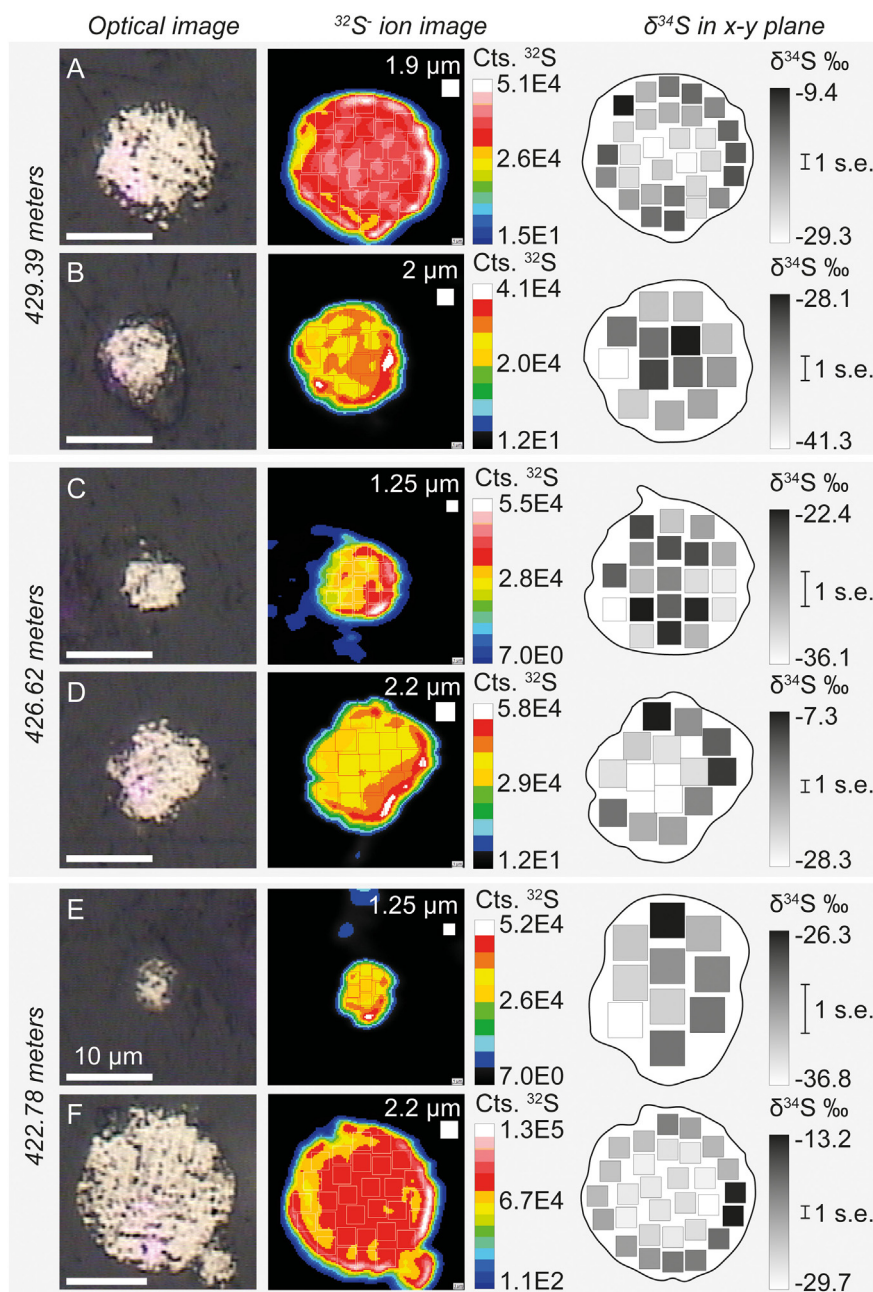


**Fig. 5.** Internal  $\delta^{34}\text{S}$  variability in framboids from (A, B) the deepest pre-OAE-2 sample, (C, D) the sample deposited slightly before OAE-2, and (E, F) the *syn*-OAE-2 sample. From left-right, panels display: optical microscope images, where scale bars are all 10  $\mu\text{m}$ ;  $^{32}\text{S}^-$  ion images, accumulated over 60–90 cycles, with inset showing the size of sub-sampled regions; and  $\delta^{34}\text{S}$  values of the sub-sampled regions, where the error bar indicates the average of the standard errors for the different sub-sampled regions.

$n = 61$ ). One larger aggregate (Fig. 6D) shows no clear spatial isotopic trend in the x-y plane (Table A3, Appendix A), whereas another large aggregate (Fig. 6E) shows very clear positive spatial autocorrelation without any radial trend (Table A3, Appendix A). The  $\delta^{34}\text{S}$  values in a smaller aggregate (Fig. 6F) are again positively spatially autocorrelated when viewed in the x-y plane but are also higher toward the grain edges (Table A3, Appendix A). Finally, in the sample deposited during OAE-2 (422.78 m), an irregular pyrite aggregate (Fig. 6G) features some intra-grain variation in  $\delta^{34}\text{S}$  ( $1\sigma = \pm 4.4\%$ , compared to an average intra-grain standard error of  $\pm 2.3\%$ ,  $1\sigma$ ,  $n = 11$ ). Viewed in the x-y plane, the aggregate is more  $^{34}\text{S}$ -enriched toward its edges (Table A3, Appendix A). Generally, where substantial isotopic variability can be discerned, it takes the form of radial (Fig. 6A, C, F, and G) or lateral/linear (Fig. 6E) enrichments in  $^{34}\text{S}$ . These patterns are representative of

the populations of irregular aggregates in all the samples studied.

**3.2.2.3. Cemented pyrite aggregate.** In the sample from within OAE-2, the single cemented pyrite aggregate for which SIMS data are available (Fig. 7A) has a large amount of intra-grain  $\delta^{34}\text{S}$  variability when viewed in the x-y plane ( $1\sigma = \pm 7.2\%$ , compared to an average intra-grain standard error of  $\pm 0.9\%$ ,  $1\sigma$ ,  $n = 26$ ). Although there is intra-grain variation in  $^{32}\text{S}^-$  ion counts, there is no trend between counts and  $\delta^{34}\text{S}$  (Fig. A5, Appendix A). The aggregate features positive spatial autocorrelation and radial  $^{34}\text{S}$ -enrichment (Table A3, Appendix A) and is more  $^{34}\text{S}$ -enriched toward its top edge (Figs. 7A; A6A, Appendix A).

**3.2.2.4. Marcasite.** Marcasite was only observed in the sample from

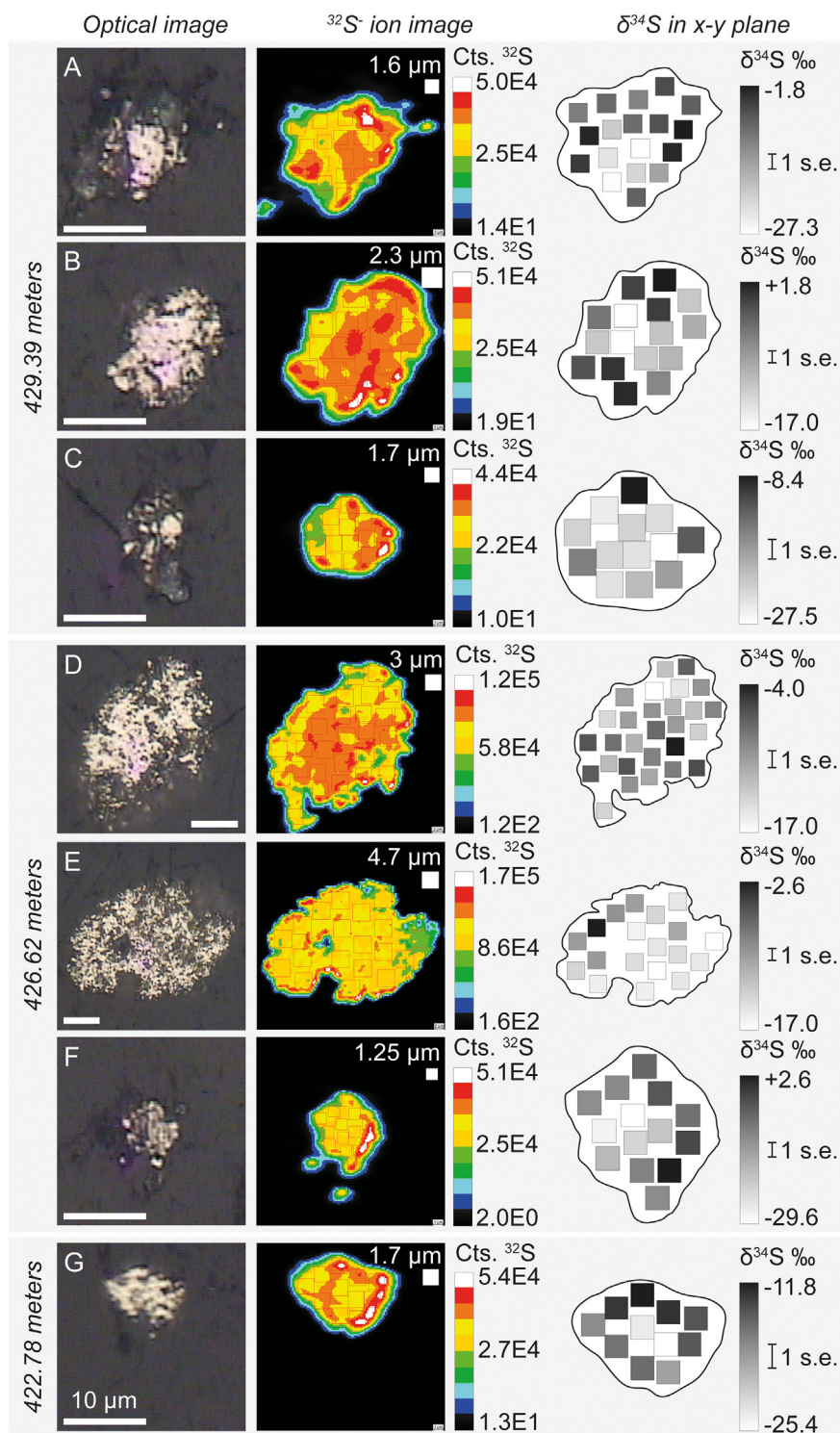


**Fig. 6.** Internal  $\delta^{34}\text{S}$  variability in irregular pyrite aggregates from (A, B, C) the deepest pre-OAE-2 sample, (D, E, F) the sample deposited slightly before OAE-2, and (G) the *syn*-OAE-2 sample. From left-right, panels display: optical microscope images, where scale bars are all 10  $\mu\text{m}$ ;  $^{32}\text{S}^-$  ion images, accumulated over 60–90 cycles, with inset showing the size of sub-sampled regions; and  $\delta^{34}\text{S}$  values of the sub-sampled regions, where the error bar indicates the average of the standard errors for the different sub-sampled regions.

within OAE-2 (422.78 m; Table 1). A cemented marcasite aggregate (perhaps a single anhedral crystal; Fig. 7B) has a large amount of intra-grain  $\delta^{34}\text{S}$  variability when viewed in the x-y plane ( $1\sigma = \pm 19.1\%$ , compared to an average intra-grain standard error of  $\pm 2.0\%$ ,  $1\sigma$ ,  $n = 16$ ), whereas the uncemented marcasite aggregate (Fig. 7C) has a lesser but still easily resolved degree of intra-grain  $\delta^{34}\text{S}$  variability ( $1\sigma = \pm 7.4\%$ , compared to an average intra-grain standard error

of  $\pm 2.2\%$ ,  $1\sigma$ ,  $n = 18$ ). Although both grains show intra-grain variation in  $^{32}\text{S}^-$  ion counts, there is no trend between counts and  $\delta^{34}\text{S}$  (Fig. A5B–C, Appendix A). The more  $^{34}\text{S}$ -enriched areas are farther from the center of the cemented marcasite aggregate (Fig. 7B; A6B, Appendix A), but closer to a central linear region of the irregular marcasite aggregate, parallel to the top/bottom edges (Fig. 7C; A6C, Appendix A). Neither grain displays autocorrelation or a simple radial

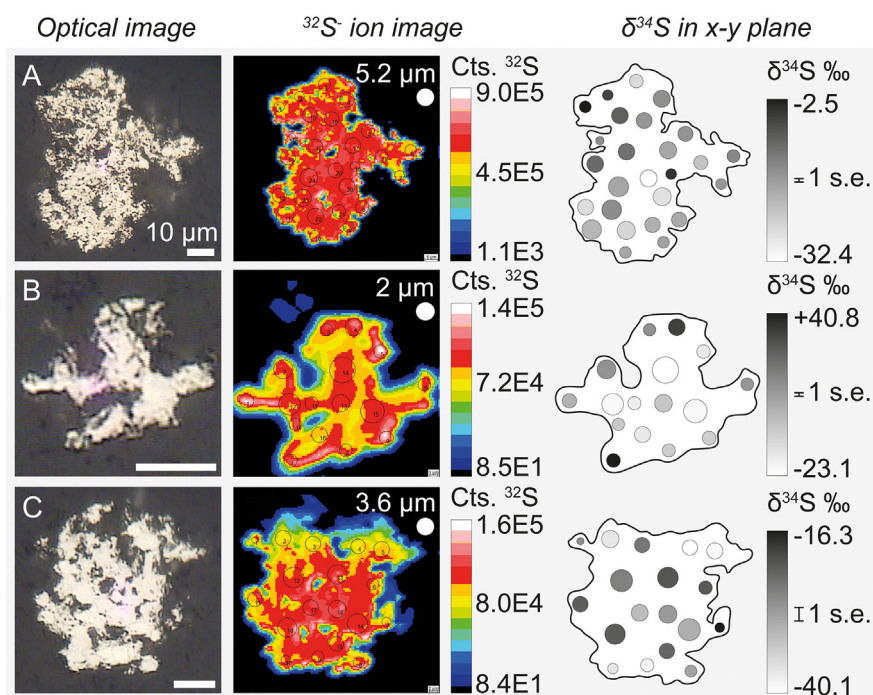


Fig. 7. Internal  $\delta^{34}\text{S}$  variability in (A) a cemented pyrite aggregate, (B) a cemented marcasite aggregate, and (C) a non-cemented marcasite aggregate, from the syn-OAE-2 sample. From left-right, panels display: optical microscope images, where scale bars are all 10  $\mu\text{m}$ ;  $^{32}\text{S}^-$  ion images, accumulated over 90–480 cycles, with inset showing the average size of sub-sampled regions; and  $\delta^{34}\text{S}$  values of sub-sampled regions, where the error bar indicates the average of the standard errors for the different sub-sampled regions.

trend (Table A3, Appendix A).

#### 4. Discussion

There are several different textures and two distinct minerals present in the Fe sulfides of the analyzed sediments of Demerara Rise, the relative proportions of which are substantially different in the syn-OAE-2 sample (Table 1; Fig. 4A). Grain-specific analyses reveal that each textural group carries a distinct average S isotopic signature (Fig. 4A), and thus any change in the proportions of these groups inevitably will result in a change of the  $\delta^{34}\text{S}_{\text{CRS}}$  value. In particular, the near-disappearance of  $^{34}\text{S}$ -enriched irregular pyrite aggregates and the appearance of large cemented aggregates are associated with the stark decrease in  $\delta^{34}\text{S}_{\text{CRS}}$  values during OAE-2 at Demerara Rise. All mineral phases and textural groups feature resolvable intra-grain variability, though the largest variability is clearly within the large aggregates (Figs. 5–7). The non-random, radial/linear spatial distribution of the intra-grain isotopic variability in many grains (Table A3, Appendix A) suggests that they formed in fluids whose isotopic compositions were evolving. This information is summarized in Fig. 8. Below we seek to address why more  $^{34}\text{S}$ -depleted S appears to have been incorporated into Fe sulfides during OAE-2 – in doing so, we integrate our results with the existing bulk  $\delta^{34}\text{S}$  records of pyrite and organic S (Hetzl et al., 2009; Raven et al., 2019).

##### 4.1. The origin of depleted $\delta^{34}\text{S}_{\text{CRS}}$ values during OAE-2

###### 4.1.1. The location of iron sulfidization

A major unknown is whether the Fe sulfides that constitute the CRS fraction of Demerara Rise sediments formed in the sediments or the water column, which is believed to have been sulfidic during the recorded interval at Demerara Rise. Pyrite framboids are documented to form in some modern sulfidic water bodies (Suits and Wilkin, 1998), though it is not clear whether this is a purely inorganic water-column process (i.e., rapid precipitation in supersaturated conditions) or to what extent it involves sulfate reduction in microenvironments in sinking organic matter-rich particles (Bianchi et al., 2018). Measurements of dissolved sulfide in modern sulfidic systems with initial sulfate concentrations similar to that of the mid-Cretaceous ocean display only

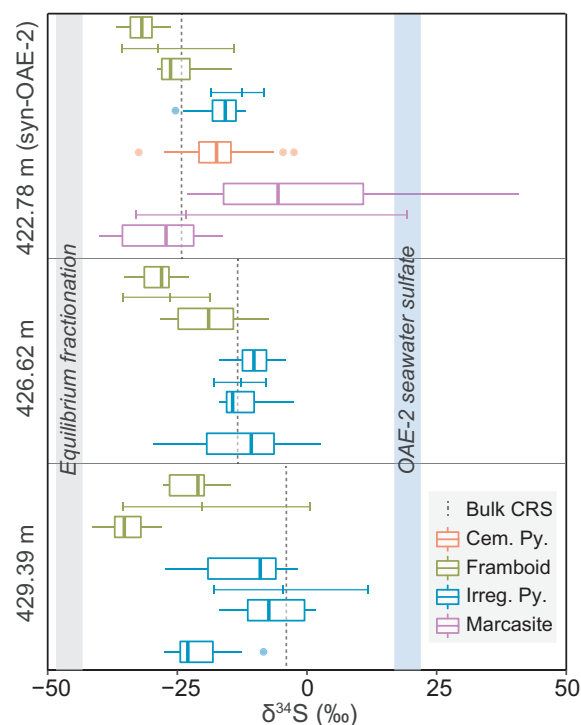


Fig. 8. Box/whisker plots (with outliers) of intra-grain  $\delta^{34}\text{S}$  observed in the x-y plane within each different Fe sulfide mineral grain featured in Figs. 5–7. The ranges record the range of pore water sulfide  $\delta^{34}\text{S}$  present during the growth of each grain. Estimates for seawater sulfate  $\delta^{34}\text{S}$  ( $\sim 19\text{‰}$  pre-OAE-2,  $\sim 19\text{--}22\text{‰}$  syn-OAE-2; Adams et al., 2010; Gomes et al., 2016; Owens et al., 2013) and equilibrium-offset sulfide  $\delta^{34}\text{S}$  at 20  $^{\circ}\text{C}$  (seawater sulfate  $\delta^{34}\text{S}$  –  $\sim 66\text{‰}$ ; Eldridge et al., 2016) are symbolized by the blue and gray bars, respectively. The black vertical dashed line represents bulk  $\delta^{34}\text{S}_{\text{CRS}}$  values, from Raven et al. (2019). Thin horizontal colored lines show the range and mean of inter-grain  $\delta^{34}\text{S}$  values for each textural group. (For interpretation of the references to colour in this figure legend, the reader is referred to the web version of this article.)

very small isotopic enrichments with depth in the water column (Gomes and Johnston, 2017). If all Fe sulfide grains were to form by the reaction of aqueous polysulfide with sinking Fe particles in a sulfidic water column, one might, therefore, expect only minimal inter- or intra-grain isotopic variability. Alternatively, if sinking particles housed both Fe and OM, sulfate reduction in microenvironments and reaction of progressively  $^{34}\text{S}$ -enriched sulfide with Fe could produce a population of Fe sulfide grains featuring intra- and/or inter-grain isotopic variability (Louca and Crowe, 2017). A similar pattern could be expected for Fe sulfide grains formed in sediment pore waters, due to the progressive consumption and isotopic enrichment of residual sulfate, albeit on a much slower timescale. Additionally, such sedimentary pyritization could impart added isotopic variability onto any initially isotopically homogeneous water-column phase. Fe sulfide populations from all three samples studied feature substantial inter- (Fig. 4) and intra-grain (Figs. 5–8; Table A3, Appendix A) isotopic variability, the latter of which likely contributed to the former, especially for framboids (Fig. A3, Appendix A). Therefore, the original Fe sulfides likely formed either in the water column in sinking particles hosting active sulfate reduction, or in sediment pore waters. In some cases, the original grains were progressively infilled from core-rim (see Fig. 5B for an example of incomplete infilling), which likely further increased  $\delta^{34}\text{S}$  variability by mixing primary framboids with sulfide precipitated from later,  $^{34}\text{S}$ -enriched (by Rayleigh distillation) fluids. Because both sinking particles and sediment pore waters house sulfate reduction in a (variably) diffusively limited ('closed') environment, we can use this framework to ascribe mechanisms to the decrease in  $\delta^{34}\text{S}_{\text{CRS}}$  toward the onset of OAE-2.

#### 4.1.2. The possible controls on $\delta^{34}\text{S}_{\text{CRS}}$

In a simplified framework with a constant isotopic fractionation during microbial sulfate reduction ( $\epsilon_{\text{mic}}$ ), the first Fe sulfide material to form in a partially closed system is expected to be the most  $^{34}\text{S}$ -depleted, whereas the last-formed material should be the most  $^{34}\text{S}$ -enriched due to the effects of Rayleigh distillation during sulfate reduction (Bryant et al., 2019; Jorgensen, 1979). In such a system, the primary controls on  $\delta^{34}\text{S}_{\text{CRS}}$  values are (i) the magnitude of  $\epsilon_{\text{mic}}$ , (ii) the openness of the system with respect to the diffusion of water column sulfate (Claypool, 2004), (iii) the total amount of Fe that could readily react with reduced S species to form Fe sulfides, and (iv) the relative rate/timing of the reactivity of Fe with reduced S species (Bryant et al., 2019; Fike et al., 2015; Poulton, 2003; Shawar et al., 2018). Additional factors of unknown importance for  $\delta^{34}\text{S}_{\text{CRS}}$  are ambient pH and  $E_h$ , as these may affect the saturation state of different sulfide minerals in the system, and the operation of different Fe sulfide formation pathways (Benning et al., 2000; Murovchick and Barnes, 1986; Poulton, 2003; Rickard, 1975; Wan et al., 2017).

The primary control on  $\epsilon_{\text{mic}}$  is the cell-specific rate of sulfate reduction (csSRR) (Leavitt et al., 2013; Sim et al., 2011a, 2011b), which is thought to relate to the availability of electron donors (Wing and Halevy, 2014). High  $e^-$ -donor availability would increase csSRR and decrease  $\epsilon_{\text{mic}}$ , resulting in bulk Fe sulfides that are less isotopically offset from seawater sulfate, and thus relatively more  $^{34}\text{S}$ -enriched. The environment with the highest probability of hosting these lower  $\epsilon_{\text{mic}}$  values is one with highly labile and abundant  $e^-$ -donor and no  $\text{O}_2$  or  $\text{NO}_3^-$ . Raven et al. (2019) proposed that sinking particles encountering a very shallow chemocline might be one such environment and might support relatively small  $\epsilon_{\text{mic}}$  at Demerara Rise. We use a combination of inter- and intra-grain  $\delta^{34}\text{S}$  values to test the relative contributions of the above factors (i-iv) to the previously observed changes in  $\delta^{34}\text{S}_{\text{CRS}}$  values (Hetzl et al., 2009; Raven et al., 2019).

#### 4.1.3. Changing microbial fractionation

Inter- (Fig. 4) and intra-grain data (Figs. 5–8) show that all samples have minimum grain-specific  $\delta^{34}\text{S}$  values of close to  $-40\text{‰}$ . Whether seawater sulfate had a constant  $\delta^{34}\text{S}$  value of  $\sim +19\text{‰}$  (Paytan, 2004)

or rose from  $\sim +19$  to  $\sim +22\text{‰}$  over the interval of interest (Owens et al., 2013), our data imply that  $\epsilon_{\text{mic}}$  approached equilibrium fractionation between sulfate and sulfide ( $\sim -66\text{‰}$  at the estimated temperature for bottom waters over Demerara Rise during the mid-Cretaceous climate maximum,  $\sim 20^\circ\text{C}$ ; Eldridge et al., 2016; Friedrich et al., 2012, 2008) both before and during OAE-2 in whatever environment the most  $^{34}\text{S}$ -depleted grains (framboids) formed (most likely pore waters). However, it is simultaneously possible that sulfate reduction in sinking particles was associated with a smaller  $\epsilon_{\text{mic}}$ , which contributed to the formation of a population of more  $^{34}\text{S}$ -enriched grains (i.e., the irregular pyrite aggregates). Due to the relative constancy of framboids' and irregular pyrite aggregates' average  $\delta^{34}\text{S}$  values between the three samples, there is no evidence that the average  $\epsilon_{\text{mic}}$  in a particular environment changed during OAE-2. However, it is conceivable that the integrated  $\epsilon_{\text{mic}}$  recorded by the sum of all iron sulfide textures changed, perhaps due to the primary locus of iron sulfidization shifting from sinking particles to sediment pore waters, as suggested by Raven et al. (2019).

#### 4.1.4. Changing 'system openness'

Secondly, closed-system dynamics may drive relatively  $^{34}\text{S}$ -enriched sulfide, whether in diffusively limited sinking particles or sediments. In a more closed system, the rate of sulfate reduction is high relative to the rate of diffusion of sulfate from the water column – this ensures that the isotopic composition of remaining aqueous sulfate and product sulfide become more  $^{34}\text{S}$ -enriched, resulting in a greater intra-sample range of preserved Fe sulfide  $\delta^{34}\text{S}$  values. If increasing system openness (i.e., slower sulfate reduction relative to the timescale of diffusion, either in sinking particles or pore waters) were responsible for the declining  $\delta^{34}\text{S}_{\text{CRS}}$  values, this would be exhibited as a narrowing range of inter- and intra-grain  $\delta^{34}\text{S}$  values toward OAE-2 (Bryant et al., 2019; Fike et al., 2015; Jorgensen, 1979). We observe no such trend within the pyrites. In fact, the addition of marcasite to the Fe sulfide pool during OAE-2 served to increase the range of preserved  $\delta^{34}\text{S}$  values to include strongly positive values (Figs. 4A, 8). In addition, non-random intra-grain  $\delta^{34}\text{S}$  heterogeneities (e.g., radial and bidirectional  $^{34}\text{S}$ -enrichments, and positive spatial autocorrelation; Figs. 5–7; Table A3 and Fig. A6, Appendix A) suggest that most Fe sulfides in all three samples formed under at least partially closed-system conditions where sulfate was being consumed by microbial sulfate reduction faster than it could be replenished by diffusion of sulfate from the water column. Therefore, consistent with prior interpretations of local redox state, our grain-specific data enable us to rule out increasing system openness (e.g., due to a shoaling of the chemocline in the sediments) as the mechanism responsible for the declining  $\delta^{34}\text{S}_{\text{CRS}}$  values leading into OAE-2.

#### 4.1.5. Changing Fe delivery

Total Fe abundance (i.e., delivery) is the third factor that can impact  $\delta^{34}\text{S}_{\text{CRS}}$  values. If the supply of reactive Fe-bearing minerals is exhausted while the concentration of sulfate in the system is still high, only very  $^{34}\text{S}$ -depleted sulfide is sequestered, resulting in very  $^{34}\text{S}$ -depleted bulk Fe sulfides (Fike et al., 2015). Assuming that there was no change in the reactivity of iron minerals reaching the site, a decrease in total Fe delivery would result in a narrowing in the range of inter- and intra-grain  $\delta^{34}\text{S}$  values toward OAE-2 (Fike et al., 2015). No such trend was observed. In addition, total Fe abundance roughly doubles during OAE-2 (Owens et al., 2012), although the median abundance of Fe sulfides in the carbonate-free fraction of sediments is similar for syn- and pre-OAE-2 sediments (Raven et al., 2019; Fig. A1, Appendix A), and iron speciation data suggests that nearly all reactive Fe is present as iron sulfides throughout the section (Owens et al., 2016). These observations suggest that the initial total abundance of Fe was not the major factor limiting  $\delta^{34}\text{S}_{\text{CRS}}$  values, and changes in this parameter were not responsible for the declining  $\delta^{34}\text{S}_{\text{CRS}}$  values prior to OAE-2.

#### 4.1.6. Changing availability of reactive Fe

A final possible explanation for the declining  $\delta^{34}\text{S}_{\text{CRS}}$  values relates to the rate/timing of Fe sulfidization (i.e., the reactivity of Fe minerals). The timescale of reactivity of Fe in the system is primarily controlled by rates of dissolution of iron minerals; these rates vary by orders of magnitude from hours (ferrihydrite) to tens of thousands of years (Fe-bearing sheet silicates) (Canfield et al., 1992; Raiswell, 1993). The S-isotope composition recorded in CRS thus integrates sulfide  $\delta^{34}\text{S}$  values across this spectrum of reactivity. Pyrite that forms from a more slowly dissolving mineral will integrate values over a larger time/depth interval. As such, more  $^{34}\text{S}$ -enriched Fe sulfides can indicate gradual release of  $\text{Fe}^{2+}$  from a less reactive mineral (Bryant et al., 2019; Shawar et al., 2018). Inter- (Fig. 4) and intra-grain (Figs. 5–8) observations show that the syn-OAE-2 sample features the largest proportion of  $^{34}\text{S}$ -depleted material, while maintaining a large intra-sample  $\delta^{34}\text{S}$  range. Additionally, inter- and intra-grain  $\delta^{34}\text{S}$  distributions for all minerals and textures in the syn-OAE-2 sample are negatively skewed (Figs. 4, 8). The near-total absence of the relatively  $^{34}\text{S}$ -enriched irregular pyrite aggregates (Figs. 4, 8) from the syn-OAE-2 sample suggests that a change in the reactivity of available Fe minerals may have resulted in physical differences in the Fe sulfides that formed. The occurrence of marcasite suggests that the minimum pH attained in sediment pore waters was also lower during OAE-2 than before (Murowchick and Barnes, 1986; Schieber, 2011, 2007). Given the overlap between the isotopic compositions of pyrite and marcasite in the sample (Fig. 4), they likely formed in similar conditions, perhaps concurrently. However, the larger inter- and intra-grain  $\delta^{34}\text{S}$  ranges for marcasite (Figs. 8; A6, Appendix A) suggest that conditions conducive to marcasite formation (i.e., low pH) persisted for longer than those more conducive to pyrite formation. The elevated OM contents of the syn-OAE-2 sediments might have contributed to the unusually low pH inferred for this site and measured at others (e.g., off Angola; Siesser, 1978), by intensifying proton liberating metabolic activity such as fermentation (Vandewiele et al., 2009), methanogenesis (Arndt et al., 2006; Soetaert et al., 2007), and organic acid production. More acidic pore fluid conditions may be corroborated by the lower carbonate contents during the OAE.

Another possibility could be variations in the mineralogy and reactivity of Fe delivered to Demerara Rise driving changes in iron sulfide morphology and  $\delta^{34}\text{S}$  values we observe. This would be consistent with observations from the organic S system; the lack of change in the speciation and  $\delta^{34}\text{S}$  of organic S similarly argues for no major change in the distribution of sulfide and its isotopes in the environment across the onset of OAE-2 (Raven et al., 2019). The shift from more  $^{34}\text{S}$ -enriched irregular pyrite aggregates to more  $^{34}\text{S}$ -depleted morphologies (marcasite, framboids, and large, cemented pyrite aggregates) indicates a shift in the relative importance of different iron sulfidization pathways, potentially associated with different Fe precursors (Canfield et al., 1992; Raiswell, 1993).

Thus, two scenarios are feasible interpretations of the data. If framboids formed from  $^{34}\text{S}$ -depleted sulfide in the water column during OAE-2 (as indicated by their small size, Table 1; Wilkin et al., 1996), and other  $^{34}\text{S}$ -depleted morphologies formed in very shallow sediments, this would indicate a prevalence of more reactive Fe during OAE-2. In this scenario, the more  $^{34}\text{S}$ -enriched irregular pyrite aggregates would result from a closed-system sedimentary process. At the same time, the earliest-formed iron sulfides (framboids) would have retained a S-isotope composition that is more than 20‰ offset from the quantitatively dominant organic S (Fig. 2). Conversely, if the more  $^{34}\text{S}$ -depleted morphologies formed entirely in pore waters, their greater relative abundance during OAE-2 could represent a shift toward a less reactive Fe mineralogy such that water column iron sulfidization was minimized (Raven et al., 2019). The majority of  $^{34}\text{S}$ -depleted pyrite measured in the syn-OAE-2 sample is in the form of large, cemented aggregates, which is morphologically consistent with their formation within the sediments. In this scenario, the irregular pyrite aggregates that are plentiful prior to OAE-2 would be interpreted as deriving from rapid

reactions within sinking particles, though the size of these aggregates (9.5  $\mu\text{m}$  diameter on average) likely precludes water column aggregation. Despite this, the similarity between the  $\delta^{34}\text{S}$  values of irregular pyrite aggregates and organic S is consistent with their formation in a similar environment, which Raven et al. (2019) argue was most likely the water column. Irregular aggregates may thus represent accumulations of smaller particle-sourced grains that subsequently aggregated during early sedimentary processes.

#### 4.2. Why might Fe sources to Demerara Rise change at the onset of OAE-2?

Fe isotopes in Demerara Rise shales are  $\sim 0\text{‰}$ , which has been used to suggest that the dominant source of Fe to Demerara Rise was hydrothermal (mostly likely from the mid-Atlantic ridge or the Caribbean Large Igneous Province (LIP); Jenkyns, 2010), before, during and after OAE-2 (Owens et al., 2012). This still allows for a change in the mineralogy or physical characteristics of the Fe source. For example, enhanced delivery of pyrite nanoparticles (as has been observed in the modern ocean; Yücel et al., 2011) associated with increased submarine volcanic activity (e.g., at the Caribbean LIP; Owens et al., 2012), could have increased the kinetics of subsequent Fe sulfide formation at Demerara Rise by lowering the supersaturation limit in micro-niches within sediments (Harmandas et al., 1998). On the other hand, trace metals are gradually drawn down over the same time interval that  $\delta^{34}\text{S}_{\text{CRS}}$  values decline (Owens et al., 2016). This was interpreted to reflect a gradual expansion in the global areal extent of anoxic and sulfidic environments, predominately in the southern proto-North Atlantic region. This same process would be expected to also effectively remove reactive iron (Böttcher et al., 2006; Owens et al., 2016), perhaps limiting iron sulfidization to the less reactive iron minerals that reached the seafloor (Raven et al., 2019).

Another factor that could have increased the rate of Fe sulfidization at Demerara Rise during OAE-2 is pore water pH. The rate of Fe dissolution during the reaction of Fe oxyhydroxides with dissolved sulfide has been shown experimentally to be a function of pH, for example peaking at a pH of 5.5 for ferrihydrite in a seawater solution (Poulton, 2003). This low pH value is not common in marine sediment pore waters, but is notable for being close to the pH ( $\sim 5$ ) below which marcasite is expected to preferentially form over pyrite (Kitchaev and Ceder, 2016; Murowchick and Barnes, 1986). Thus, the presence of marcasite exclusively in the syn-OAE-2 sample suggests that the timescale of Fe reactivity/dissolution may have shortened in response to a decrease in pore water pH. Importantly, this work suggests the locus and mechanisms driving iron sulfide mineral formation changed across the event, which has implications for Fe delivery and pore fluid interactions as the local water column likely remained sulfidic throughout this interval.

## 5. Conclusions

We have characterized and conducted grain-specific S isotopic analyses on a diverse array of Fe sulfide minerals and textures from three samples before and during OAE-2 from Demerara Rise, using a recently developed SIMS imaging approach (Bryant et al., 2019). Four distinct Fe sulfide morphologies have distinct and relatively constant isotopic compositions. The relative proportions of these morphologies differ between the samples, and these differences in abundance appear sufficient to explain the previously reported variations in bulk  $\delta^{34}\text{S}_{\text{CRS}}$  values for the samples (Hetzl et al., 2009; Raven et al., 2019). All the textures we analyzed feature substantial intra-grain  $\delta^{34}\text{S}$  variability and therefore likely formed in a diffusively limited system, either in sinking particles or subsequently in sediment pore waters. A later generation of infilling pyrite with a more  $^{34}\text{S}$ -enriched composition served to increase inter- and intra-grain  $\delta^{34}\text{S}$  variability in framboids. The largest intragrain variability is in the cemented aggregates of pyrite and marcasite (up to  $\sim 60\text{‰}$  spread), most consistent with later, closed system

accumulation. However, variations in local  $\epsilon_{\text{mic}}$ , open-system behavior, and overall Fe flux are unable to explain the decrease in bulk  $\delta^{34}\text{S}_{\text{CRS}}$  during the ~200 kyr before OAE-2. Instead, the negative shift in  $\delta^{34}\text{S}_{\text{CRS}}$  values likely reflects a shift in the mineralogy of Fe delivered to the site and thus to the rate of  $\text{Fe}^{2+}$  dissolution and sulfidization relative to those of net sulfate reduction of OM sulfurization. This change favored the formation of  $^{34}\text{S}$ -depleted iron sulfide morphologies (marcasite, framboids, and large, cemented pyrite aggregates) while inhibiting the formation of more  $^{34}\text{S}$ -enriched irregular pyrite aggregates. Our data remain inconclusive as to whether these irregular pyrite aggregates formed within sinking particles or in deeper sediments.

Scanning ion imaging analysis of iron sulfides by SIMS produces data that makes existing bulk  $\delta^{34}\text{S}_{\text{CRS}}$  isotope data several dimensions richer. There is strong potential for attributing individual iron sulfide morphologies to specific environmental settings. As we gain greater knowledge of different iron sulfidization pathways (e.g., Wan et al., 2017) and can recognize their products morphologically or geochemically, we may be able to use this tool to reconstruct the environmental distribution of sulfide and its isotopes in unprecedented detail, while also being able to identify changes in the biogeochemical iron cycle.

### Declaration of competing interest

The authors declare that they have no known competing financial interests or personal relationships that could have appeared to influence the work reported in this paper.

### Acknowledgements

The authors thank Itay Halevy, Jeff Catalano, Jill Pasteris and the members of the Fike, Bradley and Catalano Labs at Washington University, whose enthusiastic discussions yielded improvements to this work. We are grateful to Huan Cui and two anonymous reviewers for their constructive comments that benefited this manuscript. We also thank Michael Böttcher for his thoughtful editorial handling. RNB and DAF acknowledge support from the McDonnell Center for the Space Sciences at Washington University in St. Louis. We also acknowledge funding to DAF from DOE/BER (#DE-SC0014613) and from the donors of the American Chemical Society Petroleum Research Fund (#57548-ND2) for partial support of this research. We are grateful to the IODP core repository for the provision of Demerara Rise samples (requested by JDO). JDO is supported by the National High Magnetic Field Laboratory (Tallahassee, Florida), which is funded by the National Science Foundation Cooperative Agreement No. DMR1644779 and the State of Florida.

### Appendix A. Supplementary data

Supplementary information, including Figs. A1 to A6, sample ID information (Table A1), all SIMS data (Table A2), results of statistical tests applied to intra-grain SIMS data (Table A3), a written explanation of statistical tests, and two additional references, can be found at: <https://data.mendeley.com/datasets/h6df4wckz6/1>.

### References

Adams, D.D., Hurtgen, M.T., Sageman, B.B., 2010. Volcanic triggering of a biogeochemical cascade during Oceanic Anoxic Event 2. *Nat. Geosci.* 3, 201–204. <https://doi.org/10.1038/ngeo743>.

Arndt, S., Brumsack, H.J., Wirtz, K.W., 2006. Cretaceous black shales as active bioreactors: a biogeochemical model for the deep biosphere encountered during ODP Leg 207 (Demerara Rise). *Geochim. Cosmochim. Acta* 70, 408–425. <https://doi.org/10.1016/j.gca.2005.09.010>.

Barron, E.J., 1983. A warm, equable Cretaceous: the nature of the problem. *Earth Sci. Rev.* 19, 305–338. [https://doi.org/10.1016/0012-8252\(83\)90001-6](https://doi.org/10.1016/0012-8252(83)90001-6).

Benning, L.G., Wilkin, R.T., Barnes, H.L., 2000. Reaction pathways in the Fe-S system below 100°C. *Chem. Geol.* 167, 25–51. [https://doi.org/10.1016/S0009-2541\(99\)00198-9](https://doi.org/10.1016/S0009-2541(99)00198-9).

Berelson, W.M., Morine, L., Sessions, A.L., Rollins, N., Fleming, J.C., Schwalbach, J., 2018. Santa Barbara Basin flood layers: impact on sediment diagenesis. In: *SEPM Spec. Publ. No. 110*, <https://doi.org/10.2110/sepmsp.110.11>.

Berner, R.A., 1989. Biogeochemical cycles of carbon and sulfur and their effect on atmospheric oxygen over phanerozoic time. *Glob. Planet. Change* 1, 97–122. [https://doi.org/10.1016/0921-8181\(89\)90018-0](https://doi.org/10.1016/0921-8181(89)90018-0).

Berner, R.A., 2001. Modeling atmospheric O<sub>2</sub> over Phanerozoic time. *Geochim. Cosmochim. Acta* 65, 685–694. [https://doi.org/10.1016/S0016-7037\(00\)00572-X](https://doi.org/10.1016/S0016-7037(00)00572-X).

Bianchi, D., Weber, T.S., Kiko, R., Deutsch, C., 2018. Global niche of marine anaerobic metabolisms expanded by particle microenvironments. *Nat. Geosci.* 11, 263–268. <https://doi.org/10.1038/s41561-018-0081-0>.

Böttcher, M.E., Hetzel, A., Brumsack, H.-J., 2006. Sulfur-iron-carbon geochemistry in sediments of the Demerara rise. In: *Proceedings of the Ocean Drilling Program, 207 Scientific Results*. Ocean Drilling Program. <https://doi.org/10.2973/odp.proc.nr.207.108.2006>.

Briggs, D.E.G., Bottrell, S.H., Raiswell, R., 1991. Pyritization of soft-bodied fossils: Beecher's Trilobite Bed, Upper Ordovician, New York State. *Geology* 19, 1221–1224. [https://doi.org/10.1130/0091-7613\(1991\)019<1221:POSBFB>2.3.CO;2](https://doi.org/10.1130/0091-7613(1991)019<1221:POSBFB>2.3.CO;2).

Bryant, R.N., Pasteris, J.D., Fike, D.A., 2018. Variability in the raman spectrum of unpolished growth and fracture surfaces of pyrite due to laser heating and crystal orientation. *Appl. Spectrosc.* 72, 37–47. <https://doi.org/10.1177/0003702817736516>.

Bryant, R.N., Jones, C., Raven, M.R., Gomes, M.L., Berelson, W.M., Bradley, A.S., Fike, D.A., 2019. Sulfur isotope analysis of microcrystalline iron sulfides using secondary ion mass spectrometry imaging: Extracting local paleo-environmental information from modern and ancient sediments. *Rapid Commun. Mass Spectrom.* 33, 491–502. <https://doi.org/10.1002/rcm.8375>.

Canfield, D.E., 2004. The evolution of the Earth surface sulfur reservoir. *Am. J. Sci.* 304, 839–861. <https://doi.org/10.2475/ajs.304.10.839>.

Canfield, D.E., Raiswell, R., Westrich, J.T., Reaves, C.M., Berner, R.A., 1986. The use of chromium reduction in the analysis of reduced inorganic sulfur in sediments and shales. *Chem. Geol.* 54, 149–155. [https://doi.org/10.1016/0009-2541\(86\)90078-1](https://doi.org/10.1016/0009-2541(86)90078-1).

Canfield, D.E., Raiswell, R., Bottrell, S., 1992. The reactivity of sedimentary iron minerals toward sulfide. *Am. J. Sci.* 292, 659–683. <https://doi.org/10.2475/ajs.292.9.659>.

Claypool, G.E., 2004. Ventilation of marine sediments indicated by depth profiles of pore water sulfate and  $\delta^{34}\text{S}$ . *Geochem. Soc. Spec. Publ.* 9, 59–65. [https://doi.org/10.1016/S1873-9881\(04\)80007-5](https://doi.org/10.1016/S1873-9881(04)80007-5).

Cui, H., Brussel, V.U., Kitajima, K., Fournelle, J., Ishida, A., 2018. Questioning the biogenicity of neoproterozoic superheavy pyrite by SIMS. *Am. Mineral.* 103, 1362–1400. <https://doi.org/10.2138/am-2018-6489>.

Dickson, A.J., Jenkyns, H.C., Porcelli, D., van den Boorn, S., Idiz, E., 2016. Basin-scale controls on the molybdenum-isotope composition of seawater during Oceanic Anoxic Event 2 (Late Cretaceous). *Geochim. Cosmochim. Acta* 178, 291–306. <https://doi.org/10.1016/j.gca.2015.12.036>.

Ding, T., Bai, R., Li, Y., Wan, D., Zou, X., Zhang, Q., 1999. Determination of the absolute  $^{32}\text{S}/^{34}\text{S}$  ratio of IAEA-S-1 reference material and V-CDT sulfur isotope standard. *Sci. China Ser. D Earth Sci.* 42, 45–51. <https://doi.org/10.1007/BF02878497>.

Eldridge, D.L., Guo, W., Farquhar, J., 2016. Theoretical estimates of equilibrium sulfur isotope effects in aqueous sulfur systems: highlighting the role of isomers in the sulfite and sulfoxylate systems. *Geochim. Cosmochim. Acta* 195, 171–200. <https://doi.org/10.1016/j.gca.2016.09.021>.

Erbacher, J., Friedrich, O., Wilson, P.A., Birch, H., Mutterlose, J., 2005. Stable organic carbon isotope stratigraphy across Oceanic Anoxic Event 2 of Demerara rise, western tropical Atlantic. *Geochemistry, Geophys. Geosystems* 6. <https://doi.org/10.1029/2004GC000850>.

Fike, D.A., Bradley, A.S., Rose, C.V., 2015. Rethinking the ancient sulfur cycle. *Annu. Rev. Earth Planet. Sci.* 43, 593–622. <https://doi.org/10.1146/annurev-earth-060313-054802>.

Fischer, W.W., Fike, D.A., Johnson, J.E., Raub, T.D., Guan, Y., Kirschvink, J.L., Eiler, J.M., 2014. SQUID-SIMS is a useful approach to uncover primary signals in the Archean sulfur cycle. *Proc. Natl. Acad. Sci.* 111, 5468–5473. <https://doi.org/10.1073/pnas.1322577111>.

Friedrich, O., Erbacher, J., Moriya, K., Wilson, P.A., Kuhnert, H., 2008. Warm saline intermediate waters in the Cretaceous tropical Atlantic Ocean. *Nat. Geosci.* 1, 453–457. <https://doi.org/10.1038/ngeo217>.

Friedrich, O., Norris, R.D., Erbacher, J., 2012. Evolution of middle to late Cretaceous oceans a 55 m.y. Record of Earth's temperature and carbon cycle. *Geology* 40, 107–110. <https://doi.org/10.1130/G32701.1>.

Garrels, R.M., Lerman, A., 1981. Phanerozoic cycles of sedimentary carbon and sulfur. *Proc. Natl. Acad. Sci. U. S. A.* 78, 4652–4656. <https://doi.org/10.1073/pnas.78.8.4652>.

Gomes, M.L., Johnston, D.T., 2017. Oxygen and sulfur isotopes in sulfate in modern euxinic systems with implications for evaluating the extent of euxinia in ancient oceans. *Geochim. Cosmochim. Acta* 205, 331–359. <https://doi.org/10.1016/j.gca.2017.02.020>.

Gomes, M.L., Hurtgen, M.T., Sageman, B.B., 2016. Biogeochemical sulfur cycling during Cretaceous oceanic anoxic events: a comparison of OAE1a and OAE2. *Paleoceanography* 31, 233–251. <https://doi.org/10.1002/2015PA002869>.

Harmandas, N.G., Navarro Fernandez, E., Koutsoukos, P.G., 1998. Crystal growth of pyrite in aqueous solutions. inhibition by organophosphorus compounds. *Langmuir* 14, 1250–1255. <https://doi.org/10.1021/la970354c>.

Hetzel, A., Böttcher, M.E., Wortmann, U.G., Brumsack, H.J., 2009. Paleo-redox conditions during OAE 2 reflected in demerara rise sediment geochemistry (ODP Leg 207). *Paleoceanogr. Palaeoclimatol. Palaeoecol.* 273, 302–328. <https://doi.org/10.1016/j.palaeo.2008.11.005>.

- Jarvis, I., Lignum, J.S., Gröcke, D.R., Jenkyns, H.C., Pearce, M.A., 2011. Black shale deposition, atmospheric CO<sub>2</sub> drawdown, and cooling during the cenomanian-turonian oceanic anoxic event. *Paleoceanography* 26 <https://doi.org/10.1029/2010PA002081>. n/a-n/a.
- Jenkyns, H.C., 2010. Geochemistry of oceanic anoxic events. *Geochemistry, Geophys. Geosystems* 11 <https://doi.org/10.1029/2009GC002788>. n/a-n/a.
- Jones, C., Fike, D.A., Peres, P., 2017. Investigation of the quasi-simultaneous arrival (QSA) effect on a CAMECA IMS 7f-GEO. *Rapid Commun. Mass Spectrom.* 31, 623–630. <https://doi.org/10.1002/rcm.7828>.
- Jones, C., Fike, D.A., Meyer, K.M., 2019. Secondary ion mass spectrometry methodology for isotopic ratio measurement of micro-grains in thin sections: true grain size estimation and deconvolution of inter-grain size gradients and intra-grain radial gradients. *Geostand. Geoanalytical Res.* 43, 61–76. <https://doi.org/10.1111/ggr.12247>.
- Jorgensen, B.B., 1979. A theoretical model of the stable sulfur isotope distribution in marine sediments. *Geochim. Cosmochim. Acta* 43, 363–374. [https://doi.org/10.1016/0016-7037\(79\)90201-1](https://doi.org/10.1016/0016-7037(79)90201-1).
- Kitcheav, D.A., Ceder, G., 2016. Evaluating structure selection in the hydrothermal growth of FeS<sub>2</sub> pyrite and marcasite. *Nat. Commun.* 7, 13799. <https://doi.org/10.1038/ncomms13799>.
- Kolonik, S., Sinnighe Damsté, J.S., Böttcher, M.E., Kuypers, M.M.M., Kuhnt, W., Beckmann, B., Scheeder, G., Wagner, T., 2002. Geochemical characterization of Cenomanian/Turonian black shales from the Tarfaya Basin (SW Morocco). *J. Pet. Geol.* 25, 325–350. <https://doi.org/10.1111/j.1747-5457.2002.tb00012.x>.
- Leavitt, W.D., Halevy, I., Bradley, A.S., Johnston, D.T., 2013. Influence of sulfate reduction rates on the Phanerozoic sulfur isotope record. *Proc. Natl. Acad. Sci.* 110, 11244–11249. <https://doi.org/10.1073/pnas.1218874110>.
- Louca, S., Crowe, S.A., 2017. Microscale reservoir effects on microbial sulfur isotope fractionation. *Geochim. Cosmochim. Acta* 203, 117–139. <https://doi.org/10.1016/j.gca.2017.01.007>.
- MacLeod, K.G., Martin, E.E., Blair, S.W., 2008. Nd isotopic excursion across Cretaceous ocean anoxic event 2 (Cenomanian-Turonian) in the tropical North Atlantic. *Geology* 36, 811–814. <https://doi.org/10.1130/G24999A.1>.
- Murrowick, J.B., Barnes, H.L., 1986. Marcasite precipitation from hydrothermal solutions. *Geochim. Cosmochim. Acta* 50, 2615–2629. [https://doi.org/10.1016/0016-7037\(86\)90214-0](https://doi.org/10.1016/0016-7037(86)90214-0).
- Ohfujii, H., Rickard, D., 2005. Experimental syntheses of framboids - a review. *Earth-Science Rev* 71, 147–170. <https://doi.org/10.1016/j.earscirev.2005.02.001>.
- Ostrander, C.M., Owens, J.D., Nielsen, S.G., 2017. Constraining the rate of oceanic deoxygenation leading up to a cretaceous oceanic anoxic event (OAE-2: ~94 Ma). *Sci. Adv.* 3. <https://doi.org/10.1126/sciadv.1701020>.
- Owens, J.D., Lyons, T.W., Li, X., MacLeod, K.G., Gordon, G., Kuypers, M.M.M., Anbar, A., Kuhnt, W., Severmann, S., 2012. Iron isotope and trace metal records of iron cycling in the proto-North Atlantic during the Cenomanian-Turonian oceanic anoxic event (OAE-2). *Paleoceanography* 27 <https://doi.org/10.1029/2012PA002328>. n/a-n/a.
- Owens, J.D., Gill, B.C., Jenkyns, H.C., Bates, S.M., Severmann, S., Kuypers, M.M.M., Woodfine, R.G., Lyons, T.W., 2013. Sulfur isotopes track the global extent and dynamics of euxinia during Cretaceous Oceanic Anoxic Event 2. *Proc. Natl. Acad. Sci.* 110, 18407–18412. <https://doi.org/10.1073/pnas.1305304110>.
- Owens, J.D., Reinhard, C.T., Rohrsen, M., Love, G.D., Lyons, T.W., 2016. Empirical links between trace metal cycling and marine microbial ecology during a large perturbation to Earth's carbon cycle. *Earth Planet. Sci. Lett.* 449, 407–417. <https://doi.org/10.1016/j.epsl.2016.05.046>.
- Owens, J.D., Lyons, T.W., Lowery, C.M., 2018. Quantifying the missing sink for global organic carbon burial during a Cretaceous oceanic anoxic event. *Earth Planet. Sci. Lett.* 499, 83–94. <https://doi.org/10.1016/j.epsl.2018.07.021>.
- Paytan, A., 2004. Seawater sulfur isotope fluctuations in the cretaceous. *Science* 304, 1663–1665. <https://doi.org/10.1126/science.1095258>.
- Poulton, S.W., 2003. Sulfide oxidation and iron dissolution kinetics during the reaction of dissolved sulfide with ferrihydrite. *Chem. Geol.* 202, 79–94. [https://doi.org/10.1016/S0009-2541\(03\)00237-7](https://doi.org/10.1016/S0009-2541(03)00237-7).
- Raiswell, R., 1982. Pyrite texture, isotopic composition and the availability of iron. *Am. J. Sci.* 282, 1244–1263. <https://doi.org/10.2475/ajs.282.8.1244>.
- Raiswell, R., 1993. Kinetic controls on depth variations in localised pyrite formation. *Chem. Geol.* 107, 467–469. [https://doi.org/10.1016/0009-2541\(93\)90233-9](https://doi.org/10.1016/0009-2541(93)90233-9).
- Raven, M.R., Fike, D.A., Bradley, A.S., Gomes, M.L., Owens, J.D., Webb, S.A., 2019. Paired organic matter and pyrite  $\delta^{34}\text{S}$  records reveal mechanisms of carbon, sulfur, and iron cycle disruption during Ocean Anoxic Event 2. *Earth Planet. Sci. Lett.* 512, 27–38. <https://doi.org/10.1016/j.epsl.2019.01.048>.
- Rickard, D.T., 1975. Kinetics and mechanism of pyrite formation at low temperatures. *Am. J. Sci.* 275, 636–652. <https://doi.org/10.2475/ajs.275.6.636>.
- Schieber, J., 2007. Oxidation of detrital pyrite as a cause for Marcasite Formation in marine lag deposits from the Devonian of the eastern US. *Deep. Res. Part II Top. Stud. Oceanogr.* 54, 1312–1326. <https://doi.org/10.1016/j.dsr2.2007.04.005>.
- Schieber, J., 2011. Marcasite in black shales—a mineral proxy for oxygenated bottom waters and intermittent oxidation of carbonaceous muds. *J. Sediment. Res.* 81, 447–458. <https://doi.org/10.2110/jsr.2011.41>.
- Schiffbauer, J.D., Xiao, S., Cai, Y., Wallace, A.F., Hua, H., Hunter, J., Xu, H., Peng, Y., Kaufman, A.J., 2014. A unifying model for Neoproterozoic-Palaeozoic exceptional fossil preservation through pyritization and carbonaceous compression. *Nat. Commun.* 5, 5754. <https://doi.org/10.1038/ncomms6754>.
- Schlanger, S.O., Jenkyns, H.C., 1976. Cretaceous oceanic anoxic events: causes and consequences. *Geol. en Mijnbouw/Netherlands. J. Geosci.* 55, 179–184. <https://doi.org/10.3233/BME-151338>.
- Shawar, L., Halevy, I., Said-Ahmad, W., Feinstein, S., Boyko, V., Kamysny, A., Amrani, A., 2018. Dynamics of pyrite formation and organic matter sulfurization in organic-rich carbonate sediments. *Geochim. Cosmochim. Acta* 241, 219–239. <https://doi.org/10.1016/j.gca.2018.08.048>.
- Siesser, W.G., 1978. Petrography and geochemistry of pyrite and marcasite in DSDP Leg 40 sediments. *Initial Reports Deep Sea Drill. Proj.* 38–41, 767–775.
- Sim, M.S., Bosak, T., Ono, S., 2011a. Large sulfur isotope fractionation does not require disproportionation. *Science* 333, 74–77. <https://doi.org/10.1126/science.1205103>.
- Sim, M.S., Ono, S., Donovan, K., Templer, S.P., Bosak, T., 2011b. Effect of electron donors on the fractionation of sulfur isotopes by a marine *Desulfovibrio* sp. *Geochim. Cosmochim. Acta* 75, 4244–4259. <https://doi.org/10.1016/j.gca.2011.05.021>.
- Soetaert, K., Hofmann, A.F., Middelburg, J.J., Meysman, F.J.R., Greenwood, J., 2007. Reprint of “the effect of biogeochemical processes on pH.”. *Mar. Chem.* 106, 380–401. <https://doi.org/10.1016/j.marchem.2007.06.008>.
- Suits, N.S., Wilkin, R.T., 1998. Pyrite formation in the water column and sediments of a meromictic lake. *Geology* 26, 1099–1102. [https://doi.org/10.1130/0091-7613\(1998\)026<1099:PFITWC>2.3.CO;2](https://doi.org/10.1130/0091-7613(1998)026<1099:PFITWC>2.3.CO;2).
- Trabucho Alexandre, J., Tuenter, E., Henstra, G.A., Van Der Zwan, K.J., Van De Wal, R.S.W., Dijkstra, H.A., De Boer, P.L., 2010. The mid-Cretaceous North Atlantic nutrient trap: black shales and OAEs. *Paleoceanography* 25 <https://doi.org/10.1029/2010PA001925>. n/a-n/a.
- Vandewiele, S., Cowie, G., Soetaert, K., Middelburg, J.J., 2009. Amino acid biogeochemistry and organic matter degradation state across the Pakistan margin oxygen minimum zone. *Deep. Res. Part II Top. Stud. Oceanogr.* 56, 376–392. <https://doi.org/10.1016/j.dsr2.2008.05.035>.
- Wan, M., Schröder, C., Peiffer, S., 2017. Fe(III):S(-II) concentration ratio controls the pathway and the kinetics of pyrite formation during sulfidation of ferric hydroxides. *Geochim. Cosmochim. Acta* 217, 334–348. <https://doi.org/10.1016/j.gca.2017.08.036>.
- Wilkin, R.T., Barnes, H.L., Brantley, S.L., 1996. The size distribution of framboidal pyrite in modern sediments: an indicator of redox conditions. *Geochim. Cosmochim. Acta* 60, 3897–3912. [https://doi.org/10.1016/0016-7037\(96\)00209-8](https://doi.org/10.1016/0016-7037(96)00209-8).
- Wing, B.A., Halevy, I., 2014. Intracellular metabolite levels shape sulfur isotope fractionation during microbial sulfate respiration. *Proc. Natl. Acad. Sci. U. S. A.* 111, 18116–18125. <https://doi.org/10.1073/pnas.1407502111>.
- Yücel, M., Gartman, A., Chan, C.S., Luther, G.W., 2011. Hydrothermal vents as a kinetically stable source of iron-sulphide-bearing nanoparticles to the ocean. *Nat. Geosci.* 4, 367–371. <https://doi.org/10.1038/ngeo1148>.